Improving the Stability of Nanostructured Silicon Thin Film Lithium-Ion Battery Anodes through Their Controlled Oxidation

Paul R. Abel,[†] Yong-Mao Lin,[†] Hugo Celio,[§] Adam Heller,[†] and C. Buddie Mullins[†,‡,§,*]

[†]Department of Chemical Engineering, [‡] Department of Chemistry and Biochemistry, Center for Electrochemistry, and [§]Texas Materials Institute, University of Texas at Austin, 1 University Station C0400, Austin, Texas 78712, United States

ABSTRACT

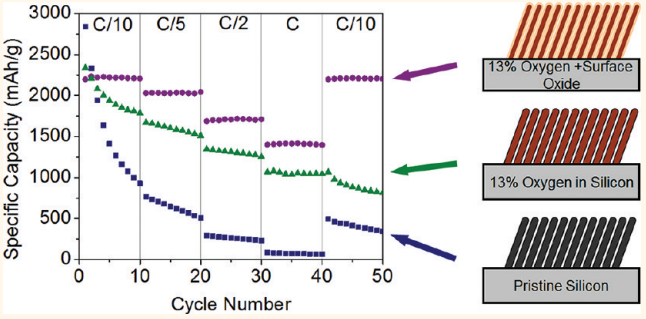

Silicon and partially oxidized silicon thin films with nanocolumnar morphology were synthesized by evaporative deposition at a glancing angle, and their performance as lithium-ion battery anodes was evaluated. The incorporated oxygen concentration was controlled by varying the partial pressure of water during the deposition and monitored by quartz crystal microbalance, X-ray photoelectron spectroscopy. In addition to bulk oxygen content, surface oxidation and annealing at low temperature affected the cycling stability and lithium-storage capacity of the films. By simultaneously optimizing all three, films of ~2200 mAh/g capacity were synthesized. Coin cells made with the optimized films were reversibly cycled for ~120 cycles with virtually no capacity fade. After 300 cycles, 80% of the initial reversible capacity was retained.

KEYWORDS: silicon · SiO_x · lithium-ion battery · nanostructured · reactive ballistic deposition

Lithium-ion batteries are widely used in portable devices and are being developed for use in zero-emission vehicles. In the latter, simultaneous demands for safety and increased energy and power density continue to outpace the improvements in battery technology. The current graphite anode is limited with respect to its safety and capacity (372 mAh/g). For this reason, a quest for superior anode materials is in progress. Silicon alloys with lithium up to $Li_{22}Si_5$, providing up to 4200 mAh/g,[1] a capacity realized in high-temperature experiments; at room temperature $Li_{15}Si_4$ (3579 mAh/g) has been reached.[2,3] Either value represents an order of magnitude improvement over the theoretical capacity of graphite anodes. The lithium insertion potential is low—~120 mV for lithiation of crystalline silicon—which allows for the construction of high-voltage (~3.8 V for a cell utilizing a $LiCoO_2$ cathode) and thusly high energy density cells. However, increased anode capacity yields diminishing returns in overall cell capacity with current cathode materials. Analysis by Kasavajjula *et al.* showed that the overall cell capacity is only marginally improved once the anode capacity is increased above ~1200 mAh/g when it is paired with a currently available high-capacity cathode (~200 mAh/g).[4] With the inherent lithium storage capacity of silicon far exceeding this value, there is excess capacity available that can be sacrificed in order to optimize other properties of the electrode, such as safety, stability, and rate capability.

The silicon-based anode has been extensively studied. Li *et al.* showed that crystalline silicon undergoes a transition to amorphous on lithium insertion; the order/disorder transition is reversible, allowing for recrystallization of the silicon upon removal of lithium.[5] Subsequent work by Hatchard and Dahn showed that this behavior was grain size dependent, that nanoscale silicon remained amorphous through the entire lithium insertion and removal cycle, and that avoiding recrystallization of the silicon extended the cycle life of the electrodes.[2] Silicon anodes can degrade rapidly by pulverization, leading to loss of electrical contact between their particles.[6] However,

* Address correspondence to mullins@che.utexas.edu.

Received for review December 14, 2011 and accepted February 28, 2012.

Published online February 28, 2012
10.1021/nn204896n

superplastically deforming small grained materials are well known. Metals that would fail at 20% elongation persevere at greater than 200% elongation when made of small grains. Consequently, it is recognized that nanoscale materials can be reversibly deformed far beyond the limit of large-grained materials.[7,8] In order to overcome the rapid loss of capacity, nanoscale silicon morphologies have been extensively investigated. The studies include nanoparticles,[9] nanorods,[10] nanowires,[11−13] nanospheres,[14] and thin films.[15,16] Despite any superplasticity imparted by the nanoscale dimensions, electrodes comprised of nanoscale silicon are still not stable. This inherent instability led Beattie *et al*. to investigate electrodes containing large concentrations of binder[17] intended to buffer the volumetric expansion associated with the lithium alloying reaction. They succeeded in reversibly cycling 100 nm silicon powder anodes by reducing the weight percentage of silicon to 33 wt %. Their electrodes, with ∼600 mAh/g capacity, were stable for 140 cycles.

Buffering the excessive expansion/shrinkage through active/inactive silicon heterostructures has also been investigated. Zhou *et al*. used a $TiSi_2$ nanonet as a silicon support.[18] This system operated reversibly as long as the lower cutoff potential was high enough to avoid the reduction of $TiSi_2$. Magasinski *et al*. used high surface area, dendritic carbon-black as a support for CVD silicon.[18,19] The electrodes cycled well for 100 cycles with a specific capacity of ∼1600 mAh/g.

Other methods for stabilizing the silicon electrode include coatings such as carbon[11,20] and copper[13] and chemical surface treatments such as hydrogen termination and ligand capping,[21] and while these do affect the lithium-storage dynamics and improve the cycle life, they are insufficient to completely stabilize the electrode.

This study considers the chemical modification of silicon by controlled oxidation. Gao *et al*. showed that SiO_2 nanoparticles react reversibly with lithium given sufficiently high potential to drive the reverse reaction.[22] Yang *et al*. showed that SiO_x ($0.8 < x < 1.1$) electrodes could be reversibly cycled, and lower oxygen content increased the reversible capacity but diminished the stability.[23] This was confirmed by Kim *et al*. for SiO_x with $0.18 < x < 0.5$.[24] Morita and Takami showed that composite electrodes of disproportionated SiO and carbon retained ∼90% of their initial ∼700 mAh/g capacity after 200 cycles.[25] Disproportionated SiO forms Si in an SiO_2 matrix, leading to active−inactive structures that help buffer the strain during cycling.[26] Additional work on SiO_x/C composites by Hu *et al*. showed that capacities of 1100 mAh/g could be realized without sacrificing stability.[27] Park *et al*. showed that the extent of disproportionation in SiO is temperature dependent, and partially disproportionated SiO provides superior performance as an anode material.[28] Yoo *et al*. reported the synthesis of Si/SiO_x core−shell structures with a reversible lithium storage capacity of ∼2000 mAh/g and good stability for 70 cycles.[29]

While disproportionation buffers the strain, the SiO_2 introduced increases the resistivity. For this reason we focus our investigation on SiO_x where $0 < x < 0.2$, avoiding the detrimental effects of excess SiO_2. In addition to the fraction of oxygen in the bulk of the films, we consider the effect of the native surface oxide on the performance of the anodes. Studies of Xun *et al*.[30] and McDowell *et al*.[31] have shown that the reversible capacity of nanoscale silicon is decreased by a thick surface oxide. This is evident also in our findings, but while McDowell *et al*. report that an oxide layer is detrimental to cycling stability, we find that an oxide layer can significantly improve the cycling stability.

In the production of silicon integrated circuits, the semiconductor industry utilizes two types of oxides: dry oxides, where the silicon is oxidized using molecular oxygen, and steam oxides, where water is used as the oxidizer. Dry oxide layers have higher density and dielectric strength and grow more slowly because of the slow diffusion of oxygen in the layers.[32] The density of the steam oxides is slightly lower because of the presence of lattice-expanding Si−H and Si−OH functions. Ionic conductivity in the expanded lattice of the steam oxide is considerably higher than that in the dry oxide. For this reason we use water as our oxidizer. We employ two related evaporative deposition techniques. Glancing angle deposition (GLAD), also known as oblique angle deposition, is vacuum evaporative deposition at high angles of incidence, where the angle controls the morphology of the resulting film.[33,34] When the angle is near normal, the films are dense. When the angles are glancing, the films are nanocolumnar. Evaporation under high vacuum onto a substrate at room temperature is a form of ballistic deposition. The presence of a reactive gas during the deposition alters the chemical composition of the deposit *via* a process known as reactive ballistic deposition (RBD).[35−39] RBD provides reproducible nanostructured morphologies with tunable composition and has been used to synthesize materials for use in energy storage[16,40] and conversion.[41,42] Our study builds on the work of Fleischauer *et al*.,[16] who deposited silicon films at glancing angles with promising results. We use RBD at glancing angles to synthesize nanostructured silicon thin films with varying oxygen content by evaporating silicon in a water ambient. The oxygen content is varied from 0 to 17 atomic % (at. %) without affecting the morphology, allowing us to separate compositional effects from structural ones. Our main finding is that by sacrificing capacity, which, for nanostructured silicon, exceeds the present battery design requirements, one can significantly enhance the cycling stability.

RESULTS AND DISCUSSION

Materials Characterization. SEM images of silicon GLAD and RBD films deposited with an incident angle of 70° are shown in Figure 1. The films are nanocolumnar, and as seen in Figure 1b, the diameter of the individual columns is on the order of 10 nm. The SEM micrograph in Figure 1c is that of a film deposited at 70° and at 2×10^{-6} Torr partial pressure H_2O and subsequently annealed to 200 °C in air for two hours. Figure 1d shows a film deposited under similar conditions, but at a partial pressure of 4×10^{-6} Torr H_2O, similarly annealed to 200 °C in air for two hours. Figure 1c and d show that the morphologies of the films deposited in a water-containing environment are not altered from that of the films deposited in the absence of water (Figure 1a and b). Oxygen incorporation in the films during their deposition and annealing increases their electrical resistance, allows their charging, and exaggerates the apparent contrast of the individual columns in Figure 1c and d. Because the structures of the films are invariant, the differences in their electrochemical behavior can be rigorously associated with changes in their composition. The porous morphology allows electrolyte to penetrate into the electrode and provides a high surface area for the reduction of lithium. Additionally, the small diameter of the individual columns minimizes the lithium diffusion length during the alloying/dealloying reaction. The high surface area is also available for native oxide formation when the films are annealed in air, and a measurable fraction of the material is oxidized during this process.

Figure 2 shows X-ray photoelectron spectra (XPS) of the silicon films. Figure 2a shows the spectra for dense films deposited at an incident angle of 0° (normal to the substrate surface) in the absence of water vapor (labeled "pristine"), with a partial pressure of 2×10^{-6} Torr H_2O, and with a partial pressure of 4×10^{-6} Torr H_2O. Because the composition of the bulk of the films is independent of the deposition angle, films deposited at normal incidence were employed so that their surface would be flat and readily cleaned by argon ion sputtering. These films were never exposed to air, and they had only a submonolayer of surface oxide when introduced into the XPS chamber. Their surface was sputtered prior to analysis in order to remove any surface contaminants. Approximately 25 nm of material was removed by the sputtering process. Quantitative analysis of the O 1s and Si 2p peaks showed the oxygen content of the pristine film to be 3 at. % (attributable to surface-adsorbed H_2O, CO, or CO_2), whereas the oxygen contents of the films deposited in a partial pressure of 2×10^{-6} and 4×10^{-6} Torr H_2O were found to be 13 and 17 at. %. Repeated sputtering of the film—removing additional material in 25 nm increments to measure the oxygen concentration at points deeper in the film—did not change the measured oxygen content, which indicates that oxygen is homogeneously incorporated into the film.

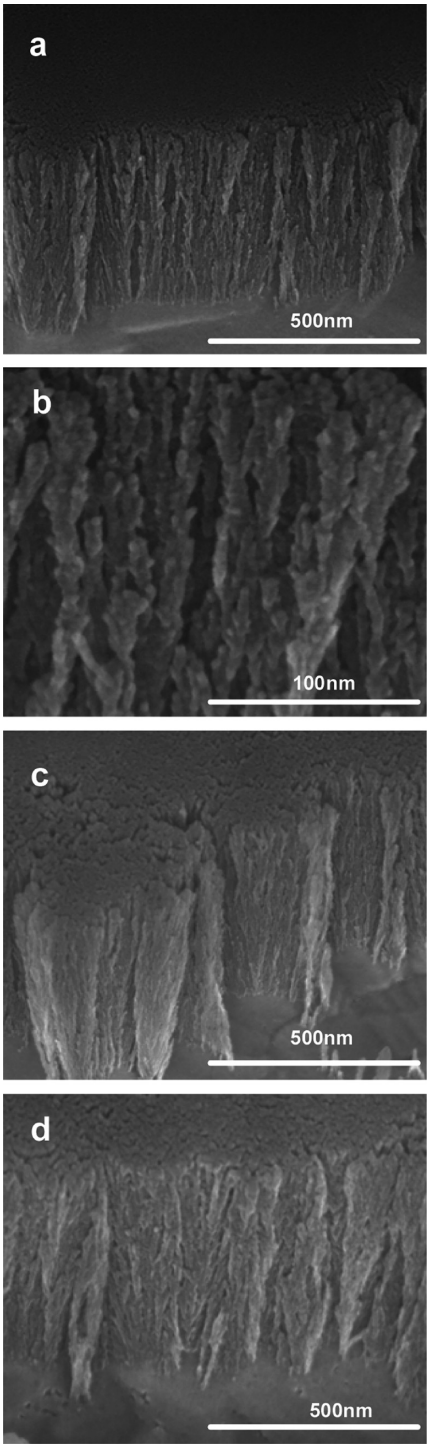

Figure 1. SEM micrographs of silicon GLAD and RBD films deposited at 70°. (a and b) Deposited in high vacuum, (c) deposited in 2×10^{-6} Torr H_2O and annealed in air at 200 °C for 2 h, and (d) deposited in 4×10^{-6} Torr H_2O and annealed in air at 200 °C for 2 h.

Irrespective of their morphologies, the oxygen content of the films was determined solely by the fluxes of silicon atoms and water molecules to the substrate during film deposition. The 13 and 17 at. % oxygen

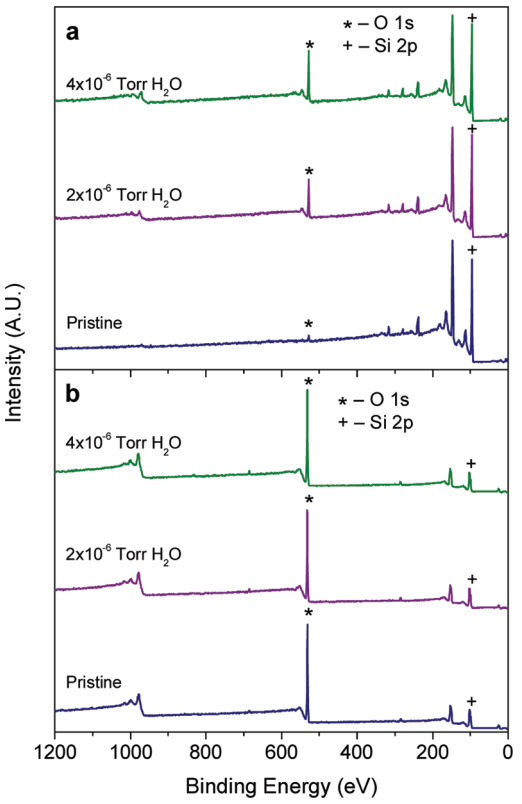

Figure 2. XPS spectra of (a) dense films grown at 0° from surface normal and lacking surface oxide and (b) films grown at 70° from surface normal and annealed in air. Quantitative analysis shows 3, 13, and 17 at. % oxygen for the pristine, 2×10^{-6} Torr H_2O, and 4×10^{-6} Torr H_2O films from (a). Analysis shows 56, 55, and 57 at. % oxygen for the vacuum deposited, 2×10^{-6} Torr H_2O, and 4×10^{-6} Torr H_2O films from (b).

content values agreed with quartz crystal microbalance (QCM)-measured deposited mass differences between silicon deposited in high vacuum at constant evaporator power and that at a particular partial pressure of water. The C 1s feature indicated 2 at. % carbon on the surface of the pristine film and 6 at. % carbon on the films deposited in 2×10^{-6} Torr H_2O and 4×10^{-6} Torr H_2O. The intensity of the carbon peak increased with the time delay between sputtering and analysis, indicating that the carbon is due to adsorbed carbon-containing species (see Figure S1). Figure 2b shows spectra for a pristine film, a film deposited in a partial pressure of 2×10^{-6} Torr H_2O, and that in a partial pressure of 4×10^{-6} Torr H_2O, but subsequently annealed in air at 200 °C for two hours. The films were deposited at 70° from surface normal. Quantitative analysis of the annealed films deposited in high vacuum (labeled "pristine"), 2×10^{-6} Torr H_2O, and 4×10^{-6} Torr H_2O shows 56, 55, and 57 at. % oxygen, respectively, on the surface of each sample. This is less than the 66 at. % expected for a silicon native oxide; however, XPS is a surface analysis technique that gathers information from the top few nanometers of the material. The thickness of a silicon native oxide

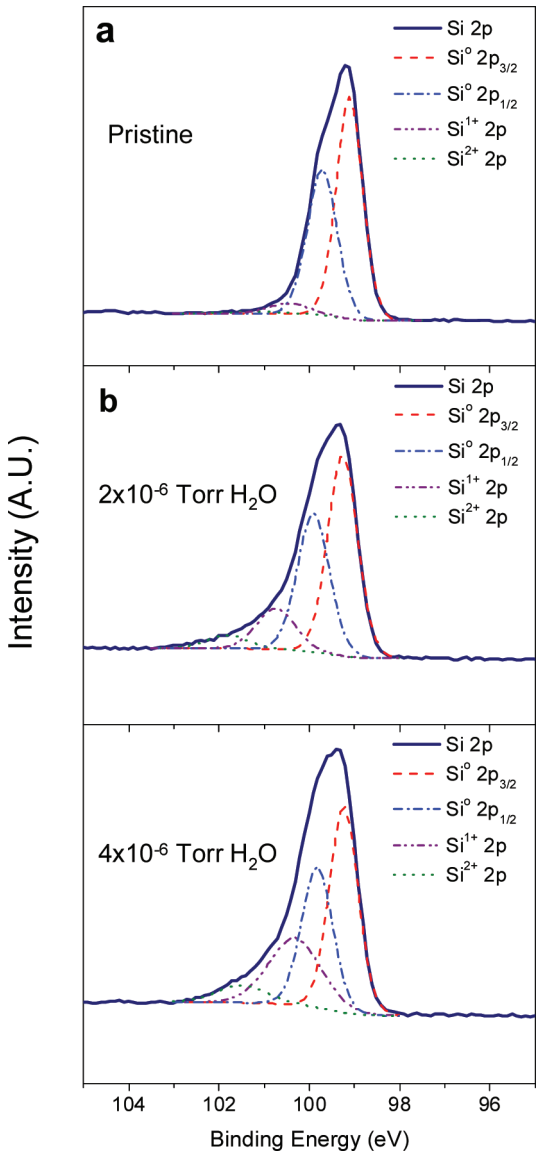

Figure 3. High-resolution XPS of the Si 2p feature of (a) pristine silicon, (b) silicon grown in 2×10^{-6} Torr H_2O, (c) silicon grown in 4×10^{-6} Torr H_2O. The fraction of silicon in the 1+ and 2+ states increases with increasing water pressure during deposition.

layer is ~1 nm, and the 200 °C anneal is not hot enough to significantly increase the thickness of this layer. The measured oxygen content determined from Figure 2b is therefore the average oxygen content of the native oxide and the material beneath it.

High-resolution measurements of the Si 2p peak show that the feature is the convolution of the Si^0, Si^+, and Si^{2+} peaks with the Si^0 peak further split due to spin–orbit coupling. Line broadening of the oxidized silicon peaks due to the amorphous nature of the material and compositional effects prevented the resolution of the individual spin states. Figure 3 shows this high-resolution measurement and the deconvolution of the measurement into its component peaks. The pristine film is nearly entirely composed of Si^0, but

as the background water pressure during deposition increases, a shoulder appears and grows in magnitude, indicating higher fractions of silicon existing in the Si^{+} and Si^{2+} states. The fraction of Si^{0} relative to Si^{+} and Si^{2+} is consistent with the QCM measurements regarding oxygen content and quantitative analysis using the O 1s feature. The lack of Si^{3+} and Si^{4+} features indicates that oxygen is incorporated randomly into the film during deposition and that the suboxide does not spontaneously disproportionate into silicon and SiO_2. Since the oxygen is incorporated randomly into the film, the probability of fully oxidizing individual silicon atoms is low. The individual components that make up the Si 2p feature are all broad, having FWHM > 0.8 eV, which is much broader than the ultimate resolution of the instrument, and is indicative of an amorphous material, as is expected for GLAD and RBD films.[36,42]

Electrochemical Characterization. Films with 100 μg total combined mass of silicon and oxygen grown in high vacuum and at 2×10^{-6} Torr H_2O or at 4×10^{-6} Torr H_2O were transferred from the vacuum chamber to a glovebox without exposure to air in a sealed vacuum transfer interface, where they were then assembled into coin cells. XPS measurements indicate that this transfer method allowed only a submonolayer surface oxide to form on these samples before assembly into coin cells. Once assembled, the cells were cycled at constant current for 10 cycles at C/10 followed by 10 cycles each at C/5, C/2, and C and then a final 10 cycles at C/10. The lithium storage capacity as a function of cycle number is shown in Figure 4. The pristine film, deposited in high vacuum without exposure to water, had a first cycle lithium insertion capacity of 3966 mAh/g. This is above the theoretical capacity for silicon at room temperature, but some charge is consumed in the first cycle by parasitic side reactions such as solid electrolyte interface (SEI) formation. The initial reversible capacity was 2839 mAh/g. This capacity had dropped to 929 mAh/g by the 10th cycle, indicating rapid degradation of the electrode. The degradation continued at the higher C-rate cycles, with a modest recovery at cycle 41. After 50 cycles, the capacity was reduced to 343 mAh/g, roughly 10% of the initial reversible capacity. The film deposited in a partial pressure of 2×10^{-6} Torr H_2O, while having a similar first cycle lithium insertion capacity, showed a slower rate of degradation, retaining a capacity of 1787 mAh/g after 10 cycles. The capacity after 50 cycles was ~812 mAh/g; however, there was very little capacity recovery when the charge/discharge rate was reduced from C to C/10. The increased oxygen content of the film deposited in a partial pressure of 4×10^{-6} Torr H_2O showed slower decay in the first 10 cycles, but the rate of degradation increased in subsequent cycles, and the capacity after 50 cycles was 507 mAh/g. This behavior suggests that, up to a point, oxygen incorporated into silicon electrodes increases their cycling stability, but is

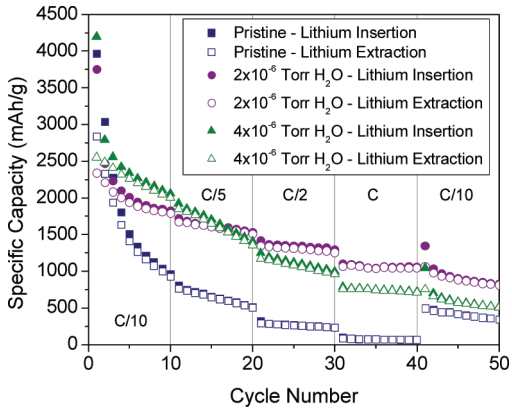

Figure 4. Silicon GLAD and RBD films deposited at 70° are cycled at various C-rates. The capacity retention is poor, with the film deposited in 2×10^{-6} Torr H_2O degrading the least.

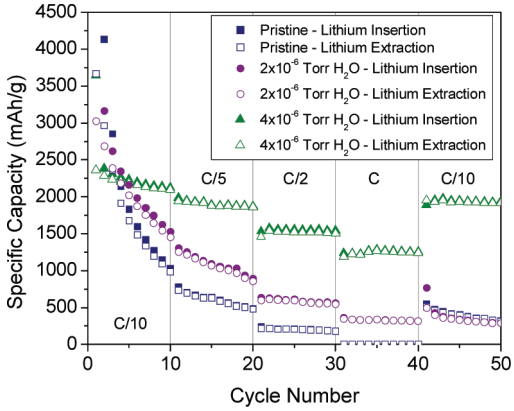

Figure 5. Silicon GLAD and RBD films deposited at 70° and annealed to 200 °C for 2 h in an inert atmosphere cycled at various C-rates. Capacity retention is better than with unannealed films, the best performing film—deposited in 4×10^{-6} Torr H_2O—retaining ~80% of its initial capacity after 50 cycles.

detrimental beyond that limit. On the basis of the oxygen content of the films deposited in 2×10^{-6} Torr H_2O and 4×10^{-6} Torr H_2O, the amount of oxygen past which the effect becomes detrimental appears to be roughly 15 at. %.

Low-temperature annealing of silicon/metal heterostructures promotes the interdiffusion of the two elements at the interface, stabilizing silicon/iron layered thin film electrodes.[43] Correspondingly, films grown in high vacuum and at a defined partial pressure of water were transferred from the vacuum chamber to the glovebox using the sealed vacuum transfer interface, but were then annealed to 200 °C for two hours in the oxygen- and water-free environment of the glovebox before being assembled into coin cells. Once assembled into coin cells, they were tested as above. The cycling data are shown in Figure 5. Surprisingly, the stability of the pristinely deposited film was not improved by the inert atmosphere annealing. After 50 cycles, the capacity was 315 mAh/g, slightly less than

the unannealed film. The film deposited in 2×10^{-6} Torr H_2O also cycled poorly. The annealing process helped to stabilize the film deposited in a partial pressure of 4×10^{-6} Torr H_2O. This electrode had an initial reversible capacity of 2362 mAh/g. After 10 cycles, the capacity had degraded to 2096 mAh/g, and the capacity was down to 1918 mAh/g after 50 cycles. The improved stability of the film deposited in a partial pressure of 4×10^{-6} Torr H_2O and the absence of improvement in films of lesser oxygen content suggest that random incorporation of oxygen is not optimal and that the higher oxidation states of silicon may stabilize the films. As seen in Figure 3, the concentration of Si^{2+} increases significantly when the pressure of water is increased from 2×10^{-6} Torr to 4×10^{-6} Torr. Low-temperature annealing may promote a structural relaxation that improves the cycling stability of the film.

In the electrode deposited in high vacuum as well as in electrodes deposited in 2×10^{-6} Torr H_2O or 4×10^{-6} Torr H_2O and annealed to 200 °C for two hours in air a native oxide layer quickly formed, but at the low annealing temperature the oxide layer thickness did not increase significantly. The films were incorporated into coin cells and tested as above. Cycling of the best performing films was continued after the 50th cycle with additional cycles performed at C/5 (Figure 6). Figure 6a shows the first 50 cycles. The film deposited in high vacuum, in the absence of water, has an initial reversible capacity of ~2720 mAh/g. The cycling stability was greatly improved over the films deposited in high vacuum and films subsequently annealed in an inert atmosphere. The capacity decayed slightly at higher C-rates but decayed rapidly beginning at cycle 41, when the C/10 rate was resumed. The film deposited at 2×10^{-6} Torr H_2O has an initial reversible capacity of ~2179 mAh/g and cycles stably for 50 cycles. The capacity fade observed in the electrode deposited in high vacuum was absent; its absence is attributed to the presence of bulk silicon suboxide formed during deposition. The film deposited in a partial pressure of 4×10^{-6} Torr H_2O shows similar qualitative behavior, but lower specific capacity. The reversible capacity is ~1696 mAh/g at C/10, but drops to ~822 mAh/g at 1C. This is a larger decrease in capacity than the film deposited in 2×10^{-6} Torr H_2O, which degreases only to ~1450 mAh/g when cycled at 1C. Figure 6b shows subsequent cycling of the films deposited in 2×10^{-6} Torr H_2O and 4×10^{-6} Torr H_2O. Cycles 51 through 300 are conducted at C/5. The capacity remained relatively constant up to about cycle 120, at which point the capacity begins to degrade. A linear fit from cycle 200 to 300 indicates that the decay rate is ~2 mAh/g per cycle, or 0.15% per cycle for the film deposited in 2×10^{-6} Torr H_2O and ~1.4 mAh/g per cycle, or 0.12% per cycle for the film deposited in 4×10^{-6} Torr H_2O. The average Coulombic efficiency for

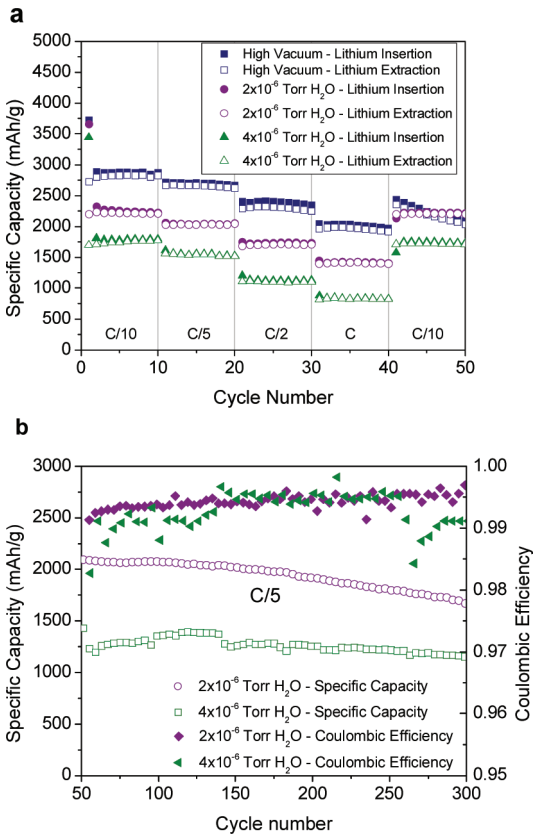

Figure 6. (a) Silicon GLAD and RBD films that have been annealed to 200 °C in air are cycled at various C-rates. (b) Cycling is continued at C/5 for the film deposited in 2×10^{-6} Torr H_2O and 4×10^{-6} Torr H_2O. The films remain stable up to cycle ~120, then degraded at ~0.15% per cycle and ~0.12% per cycle, respectively.

these cycles is ~99.5%, indicating that lithium is being consumed in parasitic side reactions on each cycle. If the SEI layer is damaged as the film expands on lithiation, the exposed electrode surface will quickly react with the electrolyte to repair the damage. As some lithium is consumed in SEI formation, this could account for the less than ideal efficiency. If this process continued, SEI material would build up in the pores of the film, eventually filling them and leading to additional stresses on the active material. This may explain the delayed onset of capacity fade in these films.

For films annealed to 200 °C for two hours in air, incorporation of oxygen during deposition decreases the capacity and extends the cycle life. Films deposited in the absence of water, and containing little bulk oxygen, have higher initial capacity, but degrade relatively quickly, while films deposited in the presence of water and containing small amounts of oxygen in the bulk are stabilized and can undergo hundreds of cycles at a slightly reduced capacity. As can be seen with the cells deposited in a partial pressure of 4×10^{-6} Torr H_2O, excessive oxygen incorporation leads to lower specific capacity. However, given that overall cell capacity does not increase significantly for anode

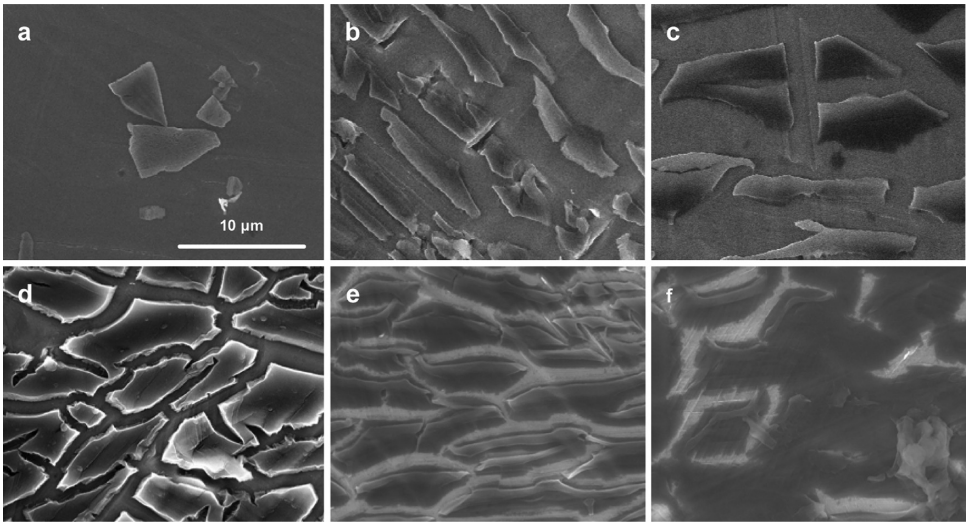

Figure 7. SEM images of silicon and partially oxidized silicon RBD electrodes after 10 cycles. (a) Pristine, (b) 2×10^{-6} Torr H_2O, and (c) 4×10^{-6} Torr H_2O without exposure to atmosphere and (d) pristine, (e) 2×10^{-6} Torr H_2O, and (f) 4×10^{-6} Torr H_2O after annealing in air at 200 °C for 2 h. The 10 μm scale bar applies to all images.

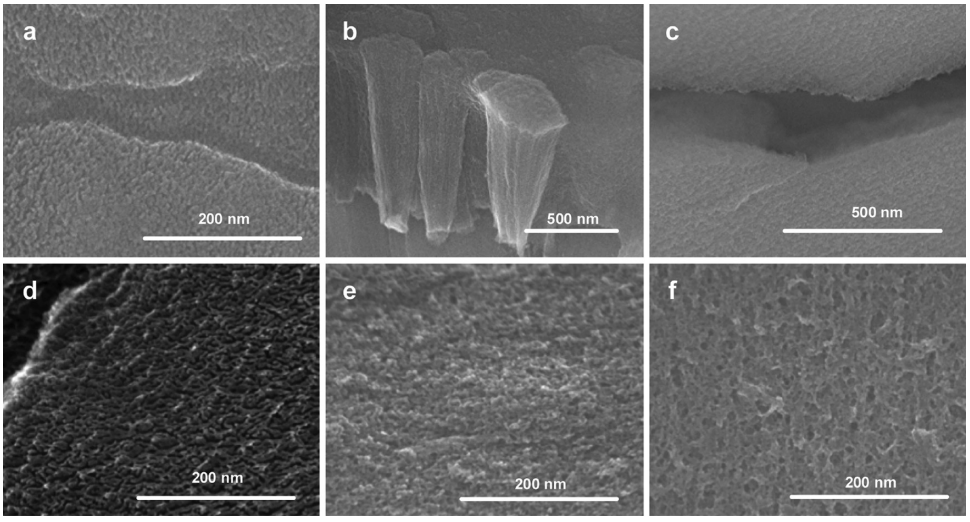

Figure 8. SEM micrographs of partially oxidized silicon RBD electrodes after 10 cycles. (a) Pristine, (b) 2×10^{-6} Torr H_2O, and (c) 4×10^{-6} Torr H_2O without exposure to atmosphere and (d) pristine, (e) 2×10^{-6} Torr H_2O, and (f) 4×10^{-6} Torr H_2O after annealing in air at 200 °C for 2 h. Despite damage to the films at the micrometer scale, nanoscale morphology is retained.

capacities above ~1200 mAh/g,[4] slightly reducing the capacity of silicon anodes in exchange for better cycle life is worthwhile with currently available cathodes.

Figure 7 shows SEM micrographs of the electrodes after 10 cycles. Figure 7a, b, and c show images of a pristine electrode and electrodes deposited in 2×10^{-6} Torr H_2O and 4×10^{-6} Torr H_2O that were assembled without exposure to atmosphere. These films exhibit significant cracking with extreme damage and almost complete loss of active material in the pristine film and slightly less damage in the oxygen-containing films. This is consistent with the capacity retained in these films after 10 cycles (see Figure 4). Figure 7d, e, and f show images of a pristine electrode and electrodes deposited in 2×10^{-6} Torr H_2O and 4×10^{-6} Torr H_2O that were annealed in air at 200 °C for two hours before assembly into coin cells. While these films still exhibit cracking, the extent of the damage is significantly less than their unannealed counterparts. The crack density is seen to decrease as the bulk oxygen content increases. The annealed films show no capacity loss after 10 cycles (see Figure 6a), indicating that, although the films are cracked, no material has become disconnected from the substrate. In addition to the lower crack density in the oxygen-containing annealed films, the active material appears to be better adhered to the substrate. In the unannealed films and the oxygen-free annealed film, shown in Figure 7a–d, the edges of silicon islands are pulled back from the substrate, indicating that they are partially delaminated. Examination of the crack edges in the partially oxidized and annealed silicon films, shown in Figure 7e

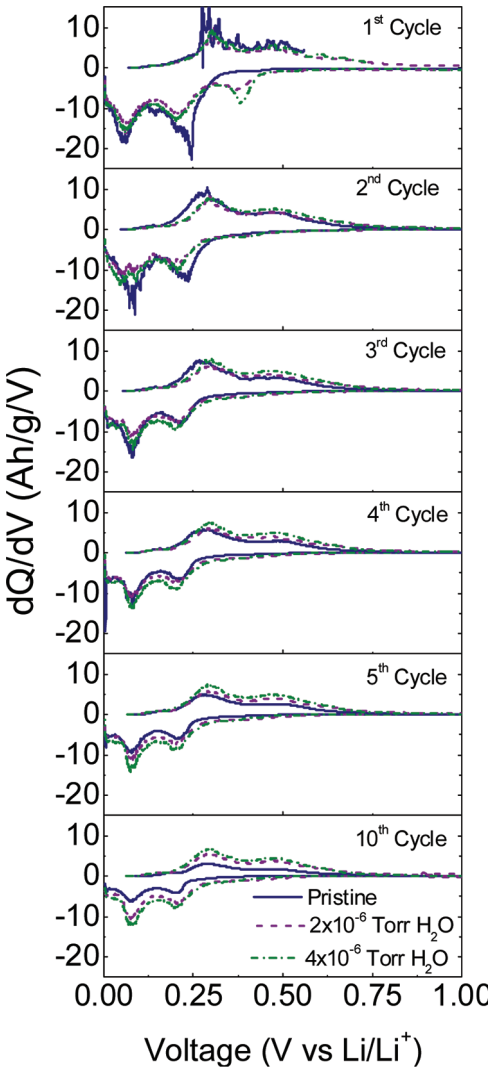

Figure 9. Differential capacity plots of silicon electrodes deposited in high vacuum, 2×10^{-6} Torr H_2O, and 4×10^{-6} Torr H_2O. The electrodes were never exposed to air. Irrespective of oxygen content, all three electrodes behave like amorphous silicon after the first cycle.

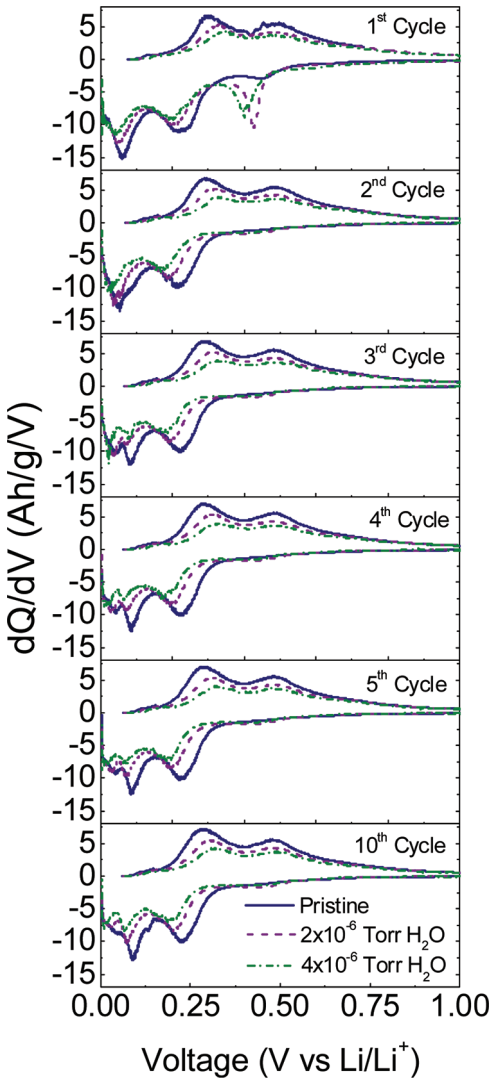

Figure 10. Differential capacity plots of silicon electrodes deposited in high vacuum, 2×10^{-6} Torr H_2O, and 4×10^{-6} Torr H_2O and subsequently annealed to 200 °C for 2 h in air. The lower voltage feature for lithium insertion into amorphous silicon splits after the second cycle. The relative intensity of the two new peaks changes in subsequent cycles. Additionally, the peak positions shift with increasing oxygen content.

and f, shows that the material remains well adhered to the substrates despite the presence of cracks in the films.

We attribute the increased stability of the partially oxidized films to three factors. First we postulate that the presence of oxygen incorporated into the film creates a lithium inactive phase that anchors the structures during cycling. This helps prevent damage during the expansion/contraction associated with cycling. Second, the presence of oxygen decreases the specific capacity of the material. Lower capacity decreases the strain during cycling and helps prevent loss of integrity at the interface with the substrate. Third, computational modeling of amorphous silicon suboxides shows that Si−O−Si bonds exhibit a wider range of bond angles than Si−Si bonds.[44] This additional conformational freedom may help to relieve stresses in the material during lithium alloying and dealloying.

Despite the damage to the films at the micrometer scale, all of the electrodes retained a nanostructured morphology after cycling, indicating that delamination from the substrate and loss of electrical contact, rather than material pulverization, is the failure mechanism in these films. High-magnification SEM micrographs of the cycled electrodes are shown in Figure 8.

Additional information is obtained by examining the cycling voltage profiles shown in differential form in Figures 9 and 10. The profiles of unannealed films (corresponding to Figure 4)—a pristine film deposited in high vacuum and films deposited in 2×10^{-6} Torr H_2O and 4×10^{-6} Torr H_2O, then transferred in the vacuum transfer interface—are shown in Figure 9. The pristine film exhibits interesting behavior on the first

cycle. It shows two broad lithium insertion features at ~100 and ~250 mV, but the higher voltage feature, while broad, had a sharp onset, attributed to the pristine nature of the film's surface. Similar behavior is seen also on the first lithium extraction cycle, a sharp onset to a broad lithium extraction feature. After the first cycle, the film shows features indicative of amorphous silicon. The intensity of the features decreases with cycling as the capacity of the film degrades (see Figure 4). Films deposited in water ambient contain an additional feature at 400 mV during the first lithium insertion. This feature is attributed to the reaction between lithium and the silicon oxide. This peak has disappeared by the second cycle, indicating that the reaction between lithium and the SiO_x species is irreversible. We conclude that this feature is due to the reaction of lithium with oxygen in the film rather than SEI formation for two reasons. First, the feature is absent in films carefully prepared without exposure to oxygen. Preventing the incorporation of oxygen into the bulk material as well as surface oxidation completely removes this feature. Second, the magnitude of this feature correlates to the bulk oxygen content of the films as measured by XPS and QCM measurements. By integrating the charge contained in this feature, the oxygen content of the films can be estimated. This charge can be related to oxygen concentration if we assume that lithium reacts with oxygen to form Li_2O. This method yields oxygen concentrations of 14 and 20 at. % for films deposited in a partial pressure of 2×10^{-6} Torr H_2O and 4×10^{-6} Torr H_2O. This is in good agreement with the XPS and QCM measurements of oxygen content (see Figure S2).

Figure 10 shows data for the films annealed to 200 °C in air (corresponding to Figure 6). The first cycle has the characteristic features of amorphous silicon plus the ~400 mV feature due to the reaction between lithium and SiO_x. Additionally, there is a tail on that feature that extends out to 900 mV due to the reaction between lithium and the native oxide layer. The magnitude of this tail increases slightly with increasing bulk oxygen content. This feature is detailed in Figure S3. As can be seen by comparing the first cycle capacity of unannealed films *versus* those of annealed films deposited under identical conditions, the presence of a native oxide layer adversely affects the magnitude of the electrode's reversible capacity.

The position of the lithium insertion and extraction features in the unannealed films (Figure 9) do not change with increasing bulk oxygen content, indicating that the presence of oxygen homogeneously incorporated into the material does not hinder electrical or ionic transport. Annealed films (Figure 10), however, exhibit peak positions that shift toward higher overpotentials with increasing oxygen content. This indicates a synergistic effect between the bulk oxygen and the surface oxide, where increased bulk oxygen increases the resistivity of the electrodes.

The features corresponding to the lithiation of SiO_x have disappeared by the second cycle, which indicates that the reaction is irreversible. The material undergoes additional irreversible changes in subsequent cycles. In the third cycle, the lower voltage lithium insertion peak splits, and the relative magnitude of the two components of this doublet shift up through the 10th cycle. This peak splitting is likely due to a symmetry breaking in the lithium storage sites due to the presence of oxygenated lithium species. The fact that the material is still changing up to the 10th cycle is interesting in that the specific capacity of the material is not changing over these cycles; therefore the changes in the insertion voltages are attributed to internal rearrangement.

CONCLUSIONS

The introduction of a small amount of oxygen (>20 at. %) during the synthesis of nanostructured silicon thin films increases their cycling stability when used as lithium-ion battery anodes. Low-temperature annealing further improves the electrode stability. The combination of homogeneous oxygen incorporation during the synthesis of the films and surface oxidation by low-temperature annealing in air provides the best cycling stability. When both bulk and surface oxides are present in an annealed film, a high capacity (2200 mAh/g) is realized with virtually no capacity loss for the first 120 cycles and slight capacity fade (~0.15% per cycle) in cycles 150–300. The electrode retains ~80% of its original capacity after 300 cycles. At a 1C rate the capacity is 1450 mAh/g. Sacrificing capacity, which, for nanostructured silicon, exceeds the present battery design requirements, one significantly enhances the cycling stability. The excellent cycling stability and high capacity make oxygen-containing silicon a promising candidate material for lithium-ion battery research.

METHODS

Film Preparation. Silicon and partially oxidized silicon films were deposited on 15.8 mm, 300 series stainless steel disks (MTI Corp.) by evaporating silicon under high vacuum (~10^{-7} Torr) or in a background of water vapor ((2–4) × 10^{-6} Torr). The vacuum chamber was first evacuated to below 5×10^{-8} Torr. The pressure rose to ~1×10^{-7} Torr when the evaporator was in use. A cylinder protruding into the chamber was filled with liquid nitrogen during deposition of unoxidized films in order to condense background water and oxygen. Quadrupole mass spectra (Stanford Research Systems, RGA200) indicate that most

of the residual gas in the chamber was hydrogen. A precision leak valve was used to backfill the chamber with water vapor up to $(2-4) \times 10^{-6}$ Torr. Total pressure was measured using a nude ionization gauge (MDC with a Stanford Research Systems controller). Silicon shot or ingot (Alfa Aesar 99.999%) was evaporated from a tantalum crucible using an electron beam evaporator (Telemark model 118). The substrate was mounted on a rotary probe, allowing the deposition angle to be adjusted between 0° and 90° (between surface normal and parallel). The crucible to substrate distance was approximately 28 cm. A quartz crystal microbalance (Inficon) was used to measure the deposition rate and the total mass of silicon deposited on a substrate. Cross sectional images of three pristine films with identical mass as measured by QCM are shown in Figure S4. The deviation in thickness between the films is quite small, only ~1%, giving confidence that the QCM is an accurate method for measuring total film mass. Once deposited, the silicon films were transferred to an argon-filled glovebox (MBraun Unilab) with oxygen content less than 0.1 ppm and water content less than 2 ppm. A sealed vacuum transfer container was used to transport some films from the vacuum chamber to the glovebox without exposure to air. Once in the glovebox, the samples were assembled into coin cells as deposited or annealed to 200 °C for two hours prior to assembly. Other samples were removed from the vacuum chamber and annealed to 200 °C for two hours in air before being introduced to the glovebox.

The QCM was also used to estimate the concentration of oxygen incorporated into the films during deposition. The mass rate of deposition was monitored as water was introduced into the chamber, and the increase in deposition rate for a given partial pressure of water was taken to be the mass of oxygen incorporated into the film. We assumed that the mass of hydrogen incorporated into the film was negligible.

Film Characterization. SEM imaging was performed using a Hitachi S-5500 scanning transmission electron microscope (STEM) using a 30 kV accelerating voltage. XPS spectra were recorded using a commercial X-ray photoelectron spectrometer (Kratos Axis Ultra), utilizing a monochromatic Al Kα X-ray source ($h\nu$ = 1486.5 eV). An automated charge neutralizer was employed for analysis. Casa XPS analysis software was used to determine the stoichiometry of samples from corrected peak areas, employing Kratos sensitivity factors for each element of interest. The analysis of films exposed to air was performed on samples deposited at 70°, but the analysis of films not exposed to air was performed on dense films, grown at normal incidence in order to allow cleaning of the surface by argon ion sputtering to better measure the true bulk composition of the material.

Transfer of samples to the XPS machine was done using the Reduce Oxidation (RoX) interface, an interface for transporting air-sensitive samples from a glovebox to an ultrahigh-vacuum chamber for X-ray photoelectron spectroscopy analysis. It was built at the Surface Analysis Laboratory of the Texas Materials Institute (TMI) at UT-Austin. The design of the interface contains a set of built-in figures of merit that were used to verify that samples were not exposed to traces of oxygen and water during transport.

Coin Cell Assembly and Electrochemical Testing. Samples were assembled into coin cells inside the glovebox. Substrates were assembled into type 2032 coin cells against a lithium metal (Alfa Aesar 99%) counter/reference electrode. The electrolyte was 5 wt % vinylene carbonate (Alfa-Aesar, 97%) added to 1 M $LiPF_6$ in 1:1 EC/DMC (EMD Chemicals). A 25 μm thick polypropylene film separator (Celgard 2400) was used. After assembly into coin cells, the electrochemical behavior of samples was tested on a multichannel battery tester (Arbin BT2143). Cells were cycled between 5 mV and 1.5 V at various currents with a 5 min rest period between charge/discharge half-cycles. Films were tested for 10 cycles at C/10 followed by 10 cycles each at C/5, C/2, and C and then a final 10 cycles at C/10 to examine how the samples recovered from the high rate tests. C-rates were calculated on the basis of a theoretical capacity of 4200 mAh/g. The best performing films were then subjected to extended cycling (300 cycles) at C/5. Electrochemical testing of some electrodes was stopped after 10 cycles. The cells were disassembled and cleaned by methods previously developed by Choi *et al.*[45] The two-step cleaning process consisted of soaking the electrode in DMC for 24 h to remove lithium salts and then dipping them in 1 mM acetic acid for 30 s to remove the SEI. The electrodes were then imaged by SEM.

Conflict of Interest: The authors declare no competing financial interest.

Acknowledgment. P.A., Y.-M.L., A.H., and C.B.M. thank the Welch Foundation (grant F-1131 for A.H. and grant F-1436 for C. B.M.) for supporting this study. P.A. also thanks the Hertz Foundation for a graduate fellowship. The authors also thank the National Science Foundation (grant no. 0618242) for funding the X-ray photoelectron spectrometer used in this work.

Supporting Information Available: Figures showing the XPS spectra of sputtered films over a two-hour period, which show the time evolution of the carbon 1s peak due to the collection of hydrocarbons on the surface of the material, EPS spectra for the first-cycle lithium insertion for annealed and unannealed films giving a detailed view of the peak attributed to the reaction between lithium and oxygen, and cross-sectional SEM images of several identical films indicating the degree of repeatability that our synthesis method allows. This material is available free of charge *via* the Internet at http://pubs.acs.org.

REFERENCES AND NOTES

1. Wen, C. J.; Huggins, R. A. Chemical Diffusion in Intermediate Phases in the Lithium-Silicon System. *J. Solid State Chem.* **1981**, *37*, 271–278.
2. Hatchard, T. D.; Dahn, J. R. *In Situ* XRD and Electrochemical Study of the Reaction of Lithium with Amorphous Silicon. *J. Electrochem. Soc.* **2004**, *151*, A838–A842.
3. Obrovac, M. N.; Christensen, L. Structural Changes in Silicon Anodes During Lithium Insertion/Extraction. *Electrochem. Solid-State Lett.* **2004**, *7*, A93–A96.
4. Kasavajjula, U.; Wang, C.; Appleby, A. J. Nano- and Bulk-Silicon-Based Insertion Anodes for Lithium-Ion Secondary Cells. *J. Power Sources* **2007**, *163*, 1003–1039.
5. Li, H.; Huang, X.; Chen, L.; Zhou, G.; Zhang, Z.; Yu, D.; Jun, M. Y.; Pei, N. The Crystal Structural Evolution of Nano-Si Anode Caused by Lithium Insertion and Extraction at Room Temperature. *Solid State Ionics* **2000**, *135*, 181–191.
6. Ryu, J. H.; Kim, J. W.; Sung, Y.-E.; Oh, S. M. Failure Modes of Silicon Powder Negative Electrode in Lithium Secondary Batteries. *Electrochem. Solid-State Lett.* **2004**, *7*, A306–A309.
7. Champion, Y.; Langlois, C.; Guérin-Mailly, S.; Langlois, P.; Bonnentien, J.-L.; Hytch, M. J. Near-Perfect Elastoplasticity in Pure Nanocrystalline Copper. *Science* **2003**, *300*, 310–311.
8. Wu, B.; Heidelberg, A.; Boland, J. J. Mechanical Properties of Ultrahigh-Strength Gold Nanowires. *Nat. Mater.* **2005**, *4*, 525–529.
9. Kim, H.; Seo, M.; Park, M.-H.; Cho, J. A Critical Size of Silicon Nano-Anodes for Lithium Rechargeable Batteries. *Angew. Chem., Int. Ed.* **2010**, *49*, 2146–2149.
10. Hieu, N. S.; Lim, J. C.; Lee, J. K. Free-Standing Silicon Nanorods on Copper Foil as Anode for Lithium-Ion Batteries. *Microelectron. Eng.* **2011**, *89*, 138–140.
11. Chan, C. K.; Patel, R. N.; O'Connell, M. J.; Korgel, B. A.; Cui, Y. Solution-Grown Silicon Nanowires for Lithium-Ion Battery Anodes. *ACS Nano* **2010**, *4*, 1443–1450.
12. Chan, C. K.; Peng, H.; Liu, G.; McIlwrath, K.; Zhang, X. F.; Huggins, R. A.; Cui, Y. High-Performance Lithium Battery Anodes Using Silicon Nanowires. *Nat. Nanotechnol.* **2008**, *3*, 31–35.
13. Chen, H.; Xiao, Y.; Wang, L.; Yang, Y. Silicon Nanowires Coated with Copper Layer as Anode Materials for Lithium-Ion Batteries. *J. Power Sources* **2011**, *196*, 6657–6662.
14. Yao, Y.; McDowell, M. T.; Ryu, I.; Wu, H.; Liu, N.; Hu, L.; Nix, W. D.; Cui, Y. Interconnected Silicon Hollow Nanospheres for Lithium-Ion Battery Anodes with Long Cycle Life. *Nano Lett.* **2011**, *11*, 2949–2954.

15. Maranchi, J. P.; Hepp, A. F.; Kumta, P. N. High Capacity, Reversible Silicon Thin-Film Anodes for Lithium-Ion Batteries. *Electrochem. Solid-State Lett.* **2003**, *6*, A198–A201.
16. Fleischauer, M. D.; Li, J.; Brett, M. J. Columnar Thin Films for Three-Dimensional Microbatteries. *J. Electrochem. Soc.* **2009**, *156*, A33–A36.
17. Beattie, S. D.; Larcher, D.; Morcrette, M.; Simon, B.; Tarascon, J. M. Si Electrodes for Li-Ion Batteries—A New Way to Look at an Old Problem. *J. Electrochem. Soc.* **2008**, *155*, A158–A163.
18. Zhou, S.; Liu, X.; Wang, D. Si/$TiSi_2$ Heteronanostructures as High-Capacity Anode Material for Li Ion Batteries. *Nano Lett.* **2010**, *10*, 860–863.
19. Magasinski, A.; Dixon, P.; Hertzberg, B.; Kvit, A.; Ayala, J.; Yushin, G. High-Performance Lithium-Ion Anodes Using a Hierarchical Bottom-Up Approach. *Nat. Mater.* **2010**, *9*, 353–358.
20. Chen, H.; Dong, Z.; Fu, Y.; Yang, Y. Silicon Nanowires With and Without Carbon Coating as Anode Materials for Lithium-Ion Batteries. *J. Solid State Electrochem.* **2010**, *14*, 1829–1834.
21. Xu, W.; Vegunta, S. S. S.; Flake, J. C. Surface-Modified Silicon Nanowire Anodes for Lithium-Ion Batteries. *J. Power Sources* **2011**, *196*, 8583–8589.
22. Gao, B.; Sinha, S.; Fleming, L.; Zhou, O. Alloy Formation in Nanostructured Silicon. *Adv. Mater.* **2001**, *13*, 816–819.
23. Yang, J.; Takeda, Y.; Imanishi, N.; Capiglia, C.; Xie, J. Y.; Yamamoto, O. SiO_x-Based Anodes for Secondary Lithium Batteries. *Solid State Ionics* **2002**, *152—153*, 125–129.
24. Kim, K.; Park, J.-H.; Doo, S.-G.; Kim, T. Effect of Oxidation on Li-Ion Secondary Battery With Non-Stoichiometric Silicon Oxide (SiO_x) Nanoparticles Generated in Cold Plasma. *Thin Solid Films* **2010**, *518*, 6547–6549.
25. Morita, T.; Takami, N. Nano Si Cluster-SiO_x-C Composite Material as High-Capacity Anode Material for Rechargeable Lithium Batteries. *J. Electrochem. Soc.* **2006**, *153*, A425–A430.
26. Wang, J.; Zhao, H.; He, J.; Wang, C.; Wang, J. Nano-Sized SiO_x/C Composite Anode for Lithium-Ion Batteries. *J. Power Sources* **2011**, *196*, 4811–4815.
27. Hu, Y.-S.; Demir-Cakan, R.; Titirici, M.-M.; Mueller, J.-O.; Schloegl, R.; Antonietti, M.; Maier, J. Superior Storage Performance of a Si@SiO_x/C Nanocomposite as Anode Material for Lithium-Ion Batteries. *Angew. Chem., Int. Ed.* **2008**, *47*, 1645–1649.
28. Park, C.-M.; Choi, W.; Hwa, Y.; Kim, J.-H.; Jeong, G.; Sohn, H.-J. Characterizations and Electrochemical Behaviors of Disproportionated SiO and Its Composite for Rechargeable Li-Ion Batteries. *J. Mater. Chem.* **2010**, *20*, 4854–4860.
29. Yoo, H.; Lee, J.-I.; Kim, H.; Lee, J.-P.; Cho, J.; Park, S. Helical Silicon/Silicon Oxide Core—Shell Anodes Grown onto the Surface of Bulk Silicon. *Nano Lett.* **2011**, *11*, 4324–4328.
30. Xun, S.; Song, X.; Grass, M. E.; Roseguo, D. K.; Liu, Z.; Battaglia, V. S.; Liu, G. Improved Initial Performance of Si Nanoparticles by Surface Oxide Reduction for Lithium-Ion Battery Application. *Electrochem. Solid-State Lett.* **2011**, *14*, A61–A63.
31. McDowell, M. T.; Lee, S. W.; Ryu, I.; Wu, H.; Nix, W. D.; Choi, J. W.; Cui, Y. Novel Size and Surface Oxide Effects in Silicon Nanowires as Lithium Battery Anodes. *Nano Lett.* **2011**, 4018–4025.
32. Ainger, F. W. The Formation and Devitrification of Oxides on Silicon. *J. Mater. Sci.* **1966**, *1*, 1–13.
33. Robbie, K.; Sit, J. C.; Brett, M. J. Advanced Techniques for Glancing Angle Deposition. *J. Vac. Sci. Technol., B* **1998**, *16*, 1115–1122.
34. Hawkeye, M. M.; Brett, M. J. Glancing Angle Deposition: Fabrication, Properties, and Applications of Micro- and Nanostructured Thin Films. *J. Vac. Sci. Technol., A* **2007**, *25*, 1317–1335.
35. Dohnálek, Z.; Kimmel, G. A.; McCready, D. E.; Young, J. S.; Dohnálková, A.; Smith, R. S.; Kay, B. D. Structural and Chemical Characterization of Aligned Crystalline Nanoporous MgO Films Grown *via* Reactive Ballistic Deposition. *J. Phys. Chem. B* **2002**, *106*, 3526–3529.
36. Flaherty, D. W.; Dohnálek, Z.; Dohnálková, A.; Arey, B. W.; McCready, D. E.; Ponnusamy, N.; Mullins, C. B.; Kay, B. D. Reactive Ballistic Deposition of Porous TiO_2 Films: Growth and Characterization. *J. Phys. Chem. C* **2007**, *111*, 4765–4773.
37. Flaherty, D. W.; Hahn, N. T.; Ferrer, D.; Engstrom, T. R.; Tanaka, P. L.; Mullins, C. B. Growth and Characterization of High Surface Area Titanium Carbide. *J. Phys. Chem. C* **2009**, *113*, 12742–12752.
38. Flaherty, D. W.; May, R. A.; Berglund, S. P.; Stevenson, K. J.; Mullins, C. B. Low Temperature Synthesis and Characterization of Nanocrystalline Titanium Carbide with Tunable Porous Architectures. *Chem. Mater.* **2009**, *22*, 319–329.
39. Flaherty, D. W.; Hahn, N. T.; May, R. A.; Berglund, S. P.; Lin, Y.-M.; Stevenson, K. J.; Dohnalek, Z.; Kay, B. D.; Mullins, C. B. Reactive Ballistic Deposition of Nanostructured Model Materials for Electrochemical Energy Conversion and Storage. *Acc. Chem. Res.*, in press, doi: 10.1021/ar200164u.
40. Lin, Y.-M.; Abel, P. R.; Flaherty, D. W.; Wu, J.; Stevenson, K. J.; Heller, A.; Mullins, C. B. Morphology Dependence of the Lithium Storage Capability and Rate Performance of Amorphous TiO_2 Electrodes. *J. Phys. Chem. C* **2011**, *115*, 2585–2591.
41. Berglund, S. P.; Flaherty, D. W.; Hahn, N. T.; Bard, A. J.; Mullins, C. B. Photoelectrochemical Oxidation of Water Using Nanostructured $BiVO_4$ Films. *J. Phys. Chem. C* **2011**, *115*, 3794–3802.
42. Hahn, N. T.; Ye, H.; Flaherty, D. W.; Bard, A. J.; Mullins, C. B. Reactive Ballistic Deposition of α-Fe_2O_3 Thin Films for Photoelectrochemical Water Oxidation. *ACS Nano* **2010**, *4*, 1977–1986.
43. Kim, J.-B.; Lee, H.-Y.; Lee, K.-S.; Lim, S.-H.; Lee, S.-M. Fe/Si Multi-Layer Thin Film Anodes for Lithium Rechargeable Thin Film Batteries. *Electrochem. Commun.* **2003**, *5*, 544–548.
44. Lee, S.; Bondi, R. J.; Hwang, G. S. *Ab Initio* Parameterized Valence Force Field for the Structure and Energetics of Amorphous SiO_x ($0<x<2$) Materials. *Phys. Rev. B* **2011**, *84*, 045202.
45. Choi, J. W.; McDonough, J.; Jeong, S.; Yoo, J. S.; Chan, C. K.; Cui, Y. Stepwise Nanopore Evolution in One-Dimensional Nanostructures. *Nano Lett.* **2010**, *10*, 1409–1413.